Powder Technology 482 (2026) 122720

Contents lists available at ScienceDirect

Powder Technology

journal homepage: www.journals.elsevier.com/powder-technology

Modelling free-flowing sodium borohydride in the dense flow regime using DEM☆

M.C. van Benten [a,*], J.T. Padding [b], D.L. Schott [a]

[a] Maritime and Transport Technology, Delft University of Technology, Mekelweg 2, 2628CD, Delft, The Netherlands
[b] Process and Energy, Delft University of Technology, Leeghwaterstraat 39, 2628CB, Delft, The Netherlands

HIGHLIGHTS

- Granular sodium borohydride can be modelled with the Hertz–Mindlin contact model.
- Rolling friction can compensate for the particle shape of sodium borohydride.
- The inertial number is shown to be spatially-dependent within a single setup.

GRAPHICAL ABSTRACT

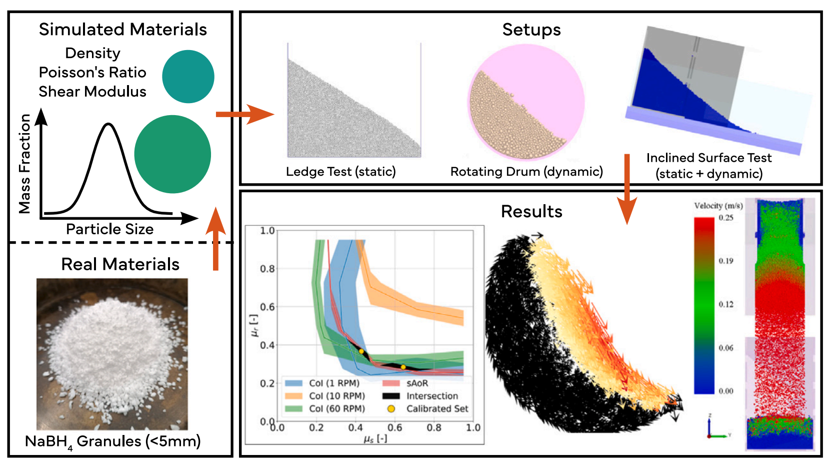

ARTICLE INFO

Keywords:
Sodium borohydride
Discrete Element Method
Inertial number
Flow regimes
Hertz–Mindlin
Rolling model C

ABSTRACT

Sodium borohydride ($NaBH_4$) is a promising hydrogen carrier for maritime applications due to its high gravimetric and volumetric energy densities compared to compressed or liquefied hydrogen. As a solid granular material, $NaBH_4$ can be stored under atmospheric pressure and room temperature, eliminating the need for extreme pressures, or cryogenic conditions. Although $NaBH_4$ is hygroscopic and can become cohesive when exposed to humid environments, when stored and handled sufficiently dry it remains free-flowing, which is essential for reliable conveying, storage, and discharge operations. Designing equipment for these processes requires an accurate understanding of $NaBH_4$'s free-flowing behaviour, motivating the need for modelling tools. To address this, we model granular, free-flowing $NaBH_4$ using the Discrete Element Method. Granular flow behaviour depends strongly on the flow regime—defined by the applied shear and confining pressure through the inertial number—and practical handling systems typically operate in the dense flow regime; consequently, this study focuses on dense-flow conditions. A standard calibration–verification–validation methodology is applied, using a ledge test and rotating drum for calibration and verification, and an inclined surface test for validation. In parallel, we evaluate the inertial number across all setups using a velocity-based approach to characterise both the global flow regime and locally occurring flow regimes within the flowing layer. Rather

☆ This article is part of a Special issue entitled: ‘DEM10’ published in Powder Technology.

* Corresponding author.
E-mail address: m.c.vanbenten@tudelft.nl (M.C. van Benten).

https://doi.org/10.1016/j.powtec.2026.122720
Received 20 March 2026; Received in revised form 7 May 2026; Accepted 25 May 2026
Available online 11 June 2026

than assigning a single characteristic value per setup, we demonstrate that distinct segments exhibit different inertial numbers, indicating that the inertial number is spatially dependent.

1. Introduction

Sodium borohydride ($NaBH_4$) is an air-stable salt increasingly considered as sustainable and renewable hydrogen carrier [1–3]. Hydrogen can be extracted by hydrolysis—a reaction with water—and its potential use on maritime vessels has attracted growing interest, resulting in research into its feasibility and performance in marine environments. For example, van Rheenen et al. [4–6] evaluate the viability and energy density of $NaBH_4$ relative to other alternative fuels, while van Benten et al. [7] focus specifically on the circular bunkering process and the adaptions required for current port and vessel infrastructures to accommodate this novel granular fuel. Moreover, they highlight the lack of data on the mechanical characteristics of $NaBH_4$, which are essential for designing the required storage and handling equipment.

In our previous work [8] we addressed this gap by experimentally quantifying the relevant mechanical characteristics required for equipment design of both $NaBH_4$ granules (<5 mm) and powder (<1 mm), including the effects of operational conditions such as humidity, temperature, and time consolidation. A key aspect of our analysis was the characterisation using three flow regimes—quasi-static flow, dense flow, and gaseous flow—as defined by [9], since all are expected in the circular bunkering process of $NaBH_4$. We found that $NaBH_4$ remains free-flowing across all regimes when stored and handled in sufficiently dry environments (relative humidity (RH) < 25% at room temperature), but can transition into a cohesive or non-flowing state due to moisture absorption or time consolidation. However, in the present work, we restrict ourselves to the dry, free-flowing state.

Despite the growing interest in $NaBH_4$, modelling of its flow behaviour remains scarcely addressed. To the best of our knowledge, only Nagar et al. [10] simulated $NaBH_4$ powder behaviour, using the Discrete Element Method (DEM). Their approach involved calibrating a single set of interaction parameters—friction, damping, and cohesion—based on wedge penetration, shear, and angle of repose tests. This calibration strategy implies a (slightly) cohesive material, which is consistent with the steep angles visible in the powder images presented in their study.

In contrast, our previous study [8] demonstrated that $NaBH_4$ exhibits free-flowing behaviour when stored and handled under dry conditions, both in powder and granular form. Moreover, we showed that granular $NaBH_4$ is less sensitive to moisture and time consolidation, making it a more suitable candidate for maritime applications. These findings reveal a clear gap in the current literature: DEM models capable of capturing the behaviour of granular, free-flowing $NaBH_4$ without relying on cohesion parameters are currently lacking.

Therefore, the aim of this study is in twofold. First, we model the free-flowing behaviour of granular sodium borohydride using the Discrete Element Method. Since bulk frictional behaviour depends on the prevailing flow regime, the present work is restricted to the dense-flow regime. To this end, we followed a standard calibration–verification–validation methodology using a ledge test and rotating drum for calibration and verification, and an inclined surface test for validation.

Second, we examine the use of the inertial number, which is typically used to classify granular flows as quasi-static, dense, or gaseous. Although granular flow studies commonly assign a single value of the inertial number to an experimental or numerical setup, we show that for the free-surface flow configuration considered here the inertial number is spatially dependent. We demonstrate that this spatial dependency can lead to variations within the flowing layer, highlighting the limitations of characterising free-surface dense flows by a single inertial number. Together with the DEM modelling of free-flowing granular $NaBH_4$, this represents a key novelty of this study.

2. Materials and experiments

This section describes the granular $NaBH_4$ used in the experiments, along with the experimental setups and results that serve as ground truth for the DEM simulations. The flow behaviour of $NaBH_4$ in the dense flow regime is characterised using three experiments: the ledge test, rotating drum, and inclined surface test. The first two experiments are described in our previous work [8], thus only the key results are shown here. The third experiment, used for validation, is discussed in more detail.

2.1. Materials

Fig. 1 shows the $NaBH_4$ granules (<5 mm) used for this study. The material was purchased from CPH Chemicals, with a reported purity exceeding 98% and moisture content below 0.3%. The particle density (1047 kg/m^3) and particle size distribution (PSD), shown in Fig. 2, were both determined in our previous study [8]. All measurements were repeated at least five times to ensure reproducibility.

2.2. Experimental results

Three different experiments are used to characterise the flow behaviour of $NaBH_4$, each providing a specific Key Performance Indicator (KPI). The ledge test yields a static AoR (sAoR), the rotating drum provides cohesive index (CoI)—defined as the temporal variation of the dynamic angle of repose (dAoR)—and the inclined surface test results in three sAoRs, measured at the top, middle, and bottom of the setup.

Ledge Test and Rotating Drum

The ledge test and rotating drum experiments—used here for calibration and verification—are described in detail in [8]; a brief summary is provided here for completeness. In the ledge test, a rectangular box (250 mm high, 183 mm long, 100 mm wide) is manually filled with 1916.7 g of granular $NaBH_4$. Near the outflow hatch at the bottom of the container, a small ledge ensures that several particle layers are always retained on the container floor. Upon opening the hatch, the material rapidly discharges, and the slope of the resulting pile is measured to determine the static angle of repose.

In the rotating drum test, a drum (20 mm wide and 84 mm in diameter), partially filled with $NaBH_4$ (fill ratio 50%–55%), is rotated at various rotational speeds while images are captured throughout the experiment. The dynamic angle of repose is defined as the average slope of the material surface during rotation. The cohesive index quantifies the variation over time of this slope relative to the dAoR, providing insights in the material's cohesiveness.

The dynamic angle of repose is, however, not used as a KPI in this study. Govender [11] noted that the dAoR can be difficult to define in rotating drums due to the characteristic S-shaped free surface. This can lead to an ill-defined dAoR, especially at higher rotational speeds where the S-shape becomes more pronounced. Moreover, only a limited section of the free surface (one–fifth of the drum diameter) is used to compute the dAoR, which further reduces its ability to describe the flow. This suggests that future work should investigate the representativeness of the dAoR for characterising flows in the rotating drum, for example by adopting a piecewise fit to the entire free surface, as proposed in our previous work [8]. Consequently, for both experiments a single KPI is extracted, and the results are summarised in Table 1.

Inclined Surface Test

Fig. 3 shows the setup of the inclined surface test—used for validation—and the measured angles. A perspex top bin (width = 68 mm, length = 100 mm) is filled with 0.5 kg $NaBH_4$. After the

List of Abbreviations and Symbols

Abbreviation	Definition
CoI	Cohesive Index
DEM	Discrete Element Method
dAoR	Dynamic Angle of Repose
HM	Hertz–Mindlin (no slip)
KPI	Key Performance Indicator
PSD	Particle Size Distribution
RH	Relative Humidity
sAoR	Static Angle of Repose

Symbol	Definition and Unit
D	Drum diameter [m]
d	Particle diameter [m]
d_v	Volume-equivalent particle diameter [m]
e	Coefficient of restitution [–]
Fr	Froude number [–]
g	Gravitational acceleration [m/s^2]
G	Shear modulus [Pa]
h	Flowing-layer thickness [m]
I	Inertial number [–]
T_R	Rayleigh time step [s]
$\bar{V}$	Mean particle velocity [m/s]
y_{DEM}	KPI from DEM simulations [–]
y_{exp}	KPI from experiments [–]
θ	Inclination angle of flowing layer [°]
μ_r	Coefficient of rolling friction [–]
μ_s	Coefficient of static friction [–]
ν	Poisson's ratio [–]
ρ	Particle density [kg/m^3]
ϕ	Particle sphericity [–]
ω	Rotational speed [rad/s]
Ψ_1	Initial heap angle [°]
Ψ_2	Bulk flow initiation angle [°]
Ψ_3	Final discharge angle [°]
Ψ_{max}	Maximum angle before collapse [°]

Fig. 1. Sample of the $NaBH_4$ granules used for this study, similar as for our previous study [8].

material has settled, an aluminium hatch is pulled upwards, allowing the material to flow into a rectangular channel, and thereby forming a stable heap with slope Ψ_1 (Fig. 3(a)). The rectangular channel consists of two parts. The first segment is 68 mm wide and 200 mm long, with a perspex bottom plate. The second segment is 74 mm wide and 212 mm long, with a stainless steel bottom plate. The side walls along both segments are made of perspex.

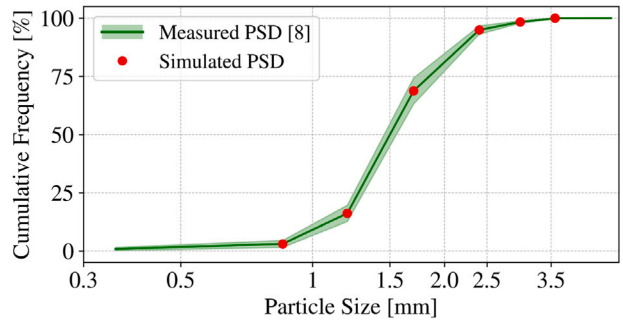

Fig. 2. Particle size distribution (PSD) of $NaBH_4$ granules measured by sieving analysis in green [8], with the red dots indicating the discrete PSD used for simulations. The green band indicates the 95% confidence interval.

Table 1
Mean values with 95% confidence intervals of experimental results of the ledge test and rotating drum, as described in [8].

Setup	KPI	Mean ± 95% CI
Ledge Test	sAoR	34.93° ± 0.31°
Rotating Drum	CoI	12.13 ± 1.3 (1 rpm) 8.70 ± 0.25 (10 rpm) 8.77 ± 0.35 (60 rpm)

The entire surface is then tilted with angular velocity ω (0.556°/s or 1.90°/s). Flow is initiated at the critical angle Ψ_2 (Fig. 3(b)). At this stage, the material does not immediately transition into a continuous discharge. Instead, the $NaBH_4$ exhibits intermittent avalanche behaviour, consisting of short flow instances followed by the formation of a temporary stable heap. For the lower tilting rate (0.556°/s), the heap typically stabilises once more after flow initiation at Ψ_2, before collapsing at a maximum angle Ψ_{max}. At the higher tilting rate (1.90°/s), the heap almost, but not fully, comes to rest between these events, resulting in a less distinct intermediate stabilisation. Consequently, Ψ_{max} could only be sharply determined for the slow tilting rate, as the heap did not fully stabilise at the faster rate. In both cases, only after the final collapse does a continuous outflow develop, such that the material flows through the rectangular channel and discharges into the receiving bin.

After the final collapse at Ψ_{max}, the resulting continuous flow propagates through the full length of the channel and discharges into a perspex receiving bin (width = 98 mm, length = 120 mm). Once the material has come to rest in the receiving bin, the final heap Ψ_3 is measured (Fig. 3(c)).

This procedure was conducted five times for each tilting rate. Previous work [8] showed that $NaBH_4$ is sensitive to changes in ambient temperature and relative humidity. To minimise the influence of these conditions (18–19 °C and 62%–63% RH) on the samples, a new sample was used for each repetition. The exposure time of each sample was limited to 15 min, and based on the moisture uptake rate measured in our previous work [8], this corresponds to a maximum moisture uptake of 0.17 wt%. This remains below the manufacturer-specified moisture content of <0.3 wt%, and therefore the samples can be considered sufficiently dry during testing.

Images of the $NaBH_4$ heaps at the top and bottom are analysed with a MATLAB script similar as used for the ledge test [8], such that Ψ_1 and Ψ_3 can be determined as the slope of the best linear fit to the material–air surface. The critical angle Ψ_2 is read from the digital display on the setup. The results are summarised in Table 2.

The difference in Ψ_2 between the two tilting rates indicates that the heap associated with angle Ψ_1 collapses earlier at higher tilting rates.

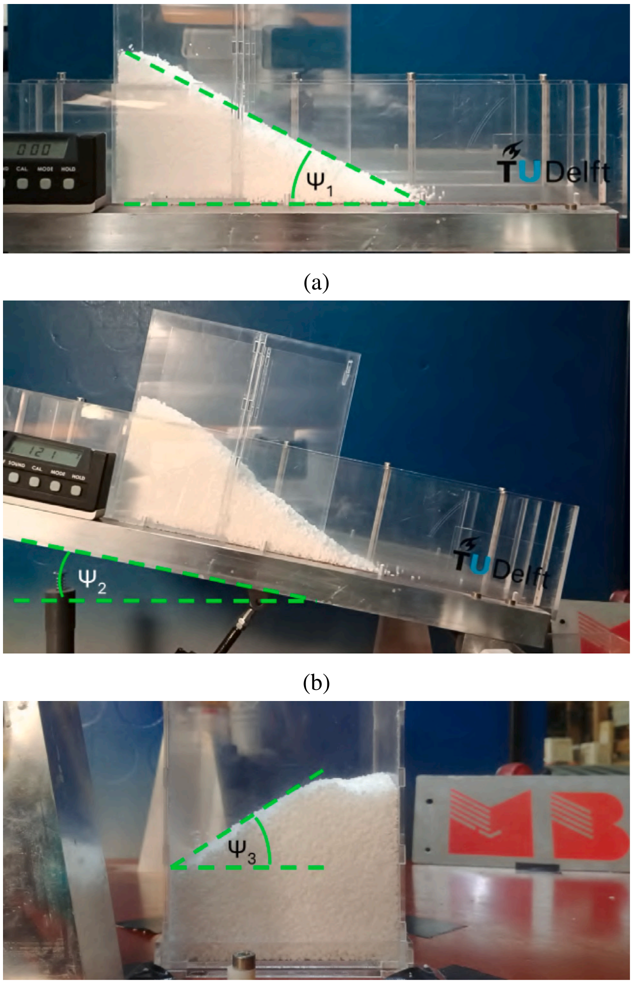

(a)
(b)
(c)

Fig. 3. Principles of the inclined surface test with (a) the angle of repose (Ψ_1), (b) the angle of bulk flow initiation* (Ψ_2), and (c) the angle of discharge (Ψ_3). Ambient conditions during experiments were measured with the Voltcraft PL-100TRH Thermo-Hygrometer at 18–19 °C and 62%–63% RH.
*: The material bed is stable until this angle, and flow initiates only after it is exceeded.

Table 2
Mean values with 95% confidence intervals of the experimental results from the inclined surface test. For Ψ_1 the full width of the heap is used, Ψ_2 is read from the digital display, and for Ψ_3 60% of the bin width was consistently used. The underlying data and analysis can be found in [12].

Tilting rate [°/s]	Angle 1 Ψ_1 [°]	Angle 2 Ψ_2 [°]	Angle 3 Ψ_3 [°]
0.556	29.15 ± 0.56	14.40 ± 3.32	35.29 ± 3.44
1.90	29.06 ± 0.38	7.88 ± 0.46	30.54 ± 1.50

We suspect this is caused by motor-induced vibrations, which may skew the results. Therefore, Ψ_2 will not be used for validation.

3. Methods

This section describes the methodology used to model $NaBH_4$ with DEM, including the governing equations of the applied contact models, the simulation settings, and the calibration–verification–validation strategy.

Fig. 4 illustrates the methodology used to calibrate, verify, and validate DEM simulations. The process starts with replicating the ledge test and rotating drum experiments from [8] in the DEM environments. Since $NaBH_4$ exhibits free-flowing behaviour, the Hertz–Mindlin (no slip) contact model was selected for both particle–particle and particle–wall interactions, and its governing equations are shown in Eqs. (1)–(9) [13]:

$$F_n = F_n^k + F_n^d \tag{1}$$

$$F_n^k = \frac{4}{3} E^* \sqrt{R^*} \delta_n^{\frac{3}{2}} \tag{2}$$

$$F_n^d = -2\sqrt{\frac{5}{6}}\beta\sqrt{k_n m^*} v_n \tag{3}$$

$$F_t = F_t^k + F_t^d \tag{4}$$

$$F_t^k = \begin{cases} k_t\delta_t, & \text{if } |k_t\delta_t| \le \mu_s F_n \\ \mu_s F_n \,\text{sign}(\delta_t), & \text{if } |k_t\delta_t| > \mu_s F_n \end{cases} \tag{5}$$

$$F_t^d = -2\sqrt{\frac{5}{6}}\beta\sqrt{k_t m^*} v_t \tag{6}$$

with

$$\beta = \frac{-\ln e}{\sqrt{\ln^2 e + \pi^2}} \tag{7}$$

$$k_n = 2\, E^* \sqrt{R^* \delta_n} \tag{8}$$

$$k_t = 8\, G^* \sqrt{R^* \delta_n} \tag{9}$$

Here, F_n and F_t denote the normal and shear force between two spheres, respectively. E^*, G^*, m^*, and R^* represent the equivalent Young's modulus, shear modulus, mass, and radius of the spheres in contact. β denotes the critical damping ratio, e the coefficient of restitution, and k_n and k_t the contact stiffness in normal and tangential directions, respectively. The relative velocity of the particles in contact is denoted by v_n (normal direction) and v_t (tangential direction). The parameter μ_s represents the coefficient of static friction (also referred to as the coefficient of sliding friction). δ_n and δ_t represent the normal and tangential overlap, respectively.

Note that the tangential overlap is not a geometric overlap similar to the normal overlap, but a history-dependent cumulative displacement that evolves over the lifetime of a contact. Finally most of these parameters depend on the particle properties and are computed internally by the simulation software; typically, only the coefficient of restitution e and coefficient of static friction μ_s are used to calibrate the Hertz–Mindlin particle interactions.

Spherical particles were used to represent the non-spherical $NaBH_4$ granules, thus a rolling model was required to compensate for the particle shape effects [14]. Rolling models A and C are the most commonly used rolling resistance models for DEM simulations [15]. Model A applies a constant opposing torque to particle motion, proportional to the particle radius, whereas model C is an elastic–plastic spring–dashpot model that allows torque to accumulate until a certain limit is reached. For this study, rolling model C was selected, as it has been shown to produce more realistic results than model A [16]. The governing equations of rolling model C are provided in Eq. (10)–(13) [13]:

$$M_r = M_r^k + M_r^d \tag{10}$$

$$M_r^k = \begin{cases} -k_r\,\theta_r, & \text{if } |k_r\,\theta_r| \le \mu_r R_r F_n \\ -\mu_r R_r F_n \,\text{sign}(\theta_r), & \text{if } |k_r\,\theta_r| > \mu_r R_r F_n \end{cases} \tag{11}$$

$$M_r^d = -2\,\eta_r\sqrt{I_r k_r}\,\boldsymbol{\omega}_r \tag{12}$$

with

$$k_r = \lambda_r k_n \mu_r^2 R_r^2 \tag{13}$$

Here, M_r denotes the total rolling resistance torque vector, consisting of a non-viscous torque contribution M_r^k and a viscous damping torque contribution M_r^d. The non-viscous torque is a function of the relative rotation angle θ_r and the rolling stiffness k_r, which is a function of a rolling stiffness coefficient λ_r, the normal contact stiffness k_n, the equivalent rolling radius R_r, and the coefficient of rolling friction μ_r. The viscous damping torque depends on the rolling viscous damping ratio η_r, the equivalent moment of inertia for rotational motion I_r, the rolling stiffness k_r, and the relative rotational velocity ω_r.

Most of these parameters are computed internally by the simulation software based on the particle properties. In practice, the rolling viscous damping ratio, rolling stiffness coefficient, and coefficient of rolling friction are commonly used to calibrate the rolling resistance behaviour. In this study, the default values of the rolling viscous damping ratio ($\eta_r = 0.3$) and the rolling stiffness coefficient ($\lambda_r = 3$) are used, while μ_r remains a free calibration parameter.

To calibrate the free-flowing behaviour using Hertz–Mindlin and Rolling Model C, the coefficient of restitution e was fixed at 0.5 for all particle–particle and particle–wall interactions, consistent with previous DEM studies of rotating drums [17–20] and inclined surface tests [21]. Additionally, sensitivity analyses in Appendices A and B showed that variations in e have minor to negligible influence on the simulated KPIs compared to the friction coefficients. The coefficient of static friction μ_s and coefficient of rolling friction μ_r for particle–wall interactions were setup-specific but held constant across simulations. The μ_s and μ_r of the particle interactions were calibrated using a full-factorial design with five levels for each parameter.

For each μ_s–μ_r combination, KPIs were extracted from the simulations: the static angle of repose from the ledge test and the cohesive index from the rotating drum (y_{DEM}), and compared with the corresponding experimental measurements (y_{exp}). Parameter sets were identified as calibrated when the simulation results satisfied the criterion $y_{DEM} \in CI_{95}(y_{exp})$ for both tests, i.e. when the (mean) simulation results reproduced the experimental data within their confidence intervals.

Since these calibrated sets were derived through interpolation between discrete simulated parameter combinations, they were re-tested in both setups to verify their accuracy. In this verification step, agreement between the simulations and experiments was assessed based on whether the results fall within, or overlap with, the experimental confidence intervals. Finally, the verified parameter set was used in an unseen experimental setup—the inclined surface test—and consecutively simulated.

The parameter set is considered validated when the relative error between simulations and experiments is less than 5%. This threshold lies within the 5%–10% range that is commonly adopted in DEM studies, and is selected here as a conservative criterion to ensure good agreement while accounting for experimental and numerical uncertainties.

3.1. DEM model setup

All DEM simulations were performed in Altair EDEM 2025.0 [22], using an NVIDIA RTX A2000 (12 GB) GPU on a Windows 10 system. Table 3 lists the DEM settings and fixed parameters, and the particle size distribution in Table 4. The particle density was measured in our previous study [8], while the Poisson's ratio (ν=0.227) and shear modulus (G=33 MPa) were taken from Ghellab et al. [23]. To reduce computational costs, the shear modulus was scaled down to 33 MPa following the approach of Lommen et al. [24].

3.2. Ledge test simulations

To reduce computational time, the original ledge test width of 100 mm was scaled down to $W/D_{50} = 10$ using periodic boundary conditions (Fig. 5), eliminating the interactions between the particles and the side walls. Due to the ledge that retains a layer of particles on the bottom, the interactions with the back plate, made of wood, remain. A time step analysis was conducted to ensure a stable time step for the calibration and verification simulations. Details regarding scaling and time stability analyses are provided in Appendix A. The simulation-specific parameters are summarised in Table 5.

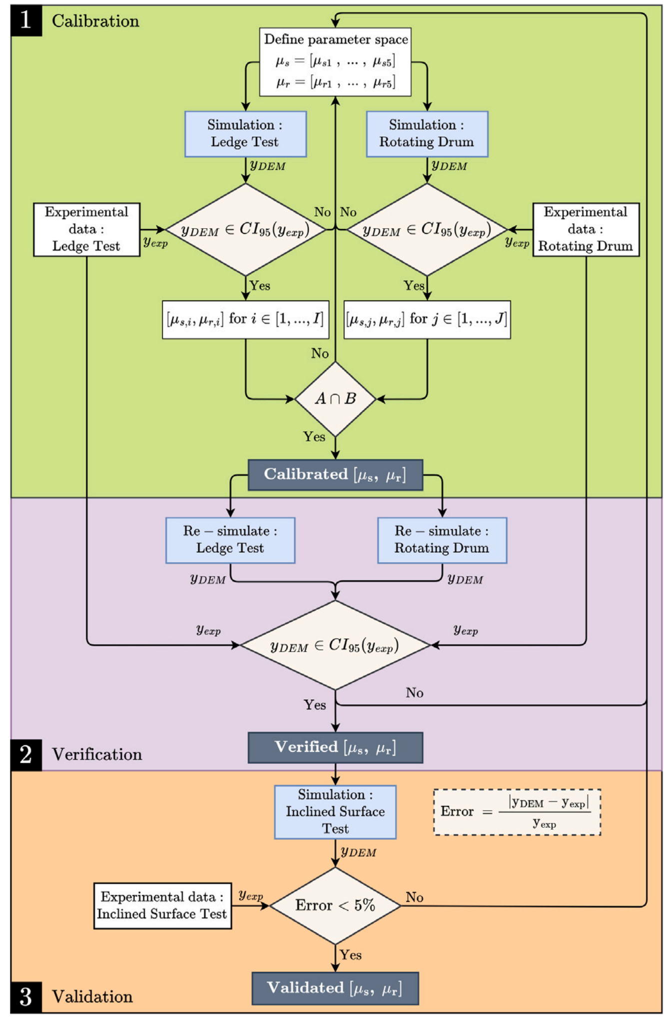

Fig. 4. Framework for the calibration, verification, and validation of particle–particle coefficients of static (μ_s) and rolling (μ_r) friction for free-flowing $NaBH_4$. The experimental data for the ledge test and the rotating drum are taken from [8], while the results of the inclined surface test are obtained in this study.

Table 3
General DEM settings and particle parameters for simulations with $NaBH_4$.

Parameter	Unit	Value
Contact Model	–	Hertz–Mindlin (no slip)
Rolling Model	–	Rolling Model C - λ_r: 3 - η_r: 0.3
Particle Density	kg/m^3	1047
Shear Modulus	MPa	33
Poisson's Ratio	–	0.227
Particle Shape	–	Sphere
Base Particle Diameter	mm	1.862
Size Distribution	–	User defined (Table 4)
Gravity	m/s^2	9.81

Table 4
Particle size distribution (mass) used for DEM simulations with $NaBH_4$. The particles are generated by multiplying the base particle diameter (Table 3) with the scaling factor.

Scaling factor [–]	Mass fraction [%]
0.459	3.061
0.644	13.134
0.913	52.559
1.289	26.184
1.598	3.433
1.920	1.629

Table 5
Ledge test simulations settings for scaled down setup.

Parameter	Unit	Value
Factory Type	–	Dynamic
Total Mass	kg	0.289
Generation Rate	kg/s	0.304
Generation Time	s	1
Settling Time	s	1
Simulation Time[a]	s	Variable
Time step[b]	% of T_R	40
	s	3.31e–06
Width/D_{50}[b]	–	10

[a] Edempy is used to run the simulations as long as required (ranging from <10 to >20 s), to ensure a stable material bed for at least 1 s before stopping.
[b] The time step and scaling analyses can be found in Appendix A.

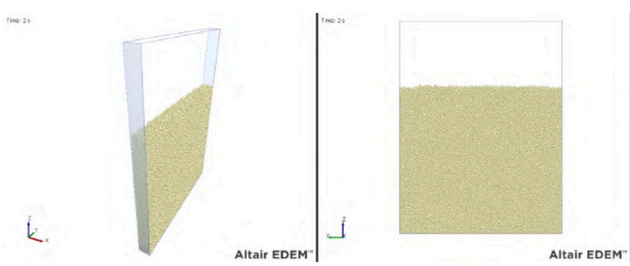

Fig. 5. Simulation setup of the scaled ledge test with periodic boundary conditions (250 mm high, 183 mm long, and 15.2 mm wide). The bottom plate is made of perspex, the back plate of wood. The setup is filled with 289 g of granular $NaBH_4$. The particle size distribution of Fig. 2 is reproduced by scaling the spherical base particle (diameter 1.862 mm) according to the scaling factors and associated mass fractions presented in Table 4.

Due to the periodic boundary conditions and the ledge geometry, particle–wall interactions only occur between particles and the back plate (wood) of the box. The coefficients μ_s and μ_r for particle–particle interactions were varied over ranges of 0.05–0.95 and 0.001–0.95, respectively, with five levels each (Table 6). This resulted in 25 unique μ_s–μ_r combinations, each simulated three times. Simulations were run with EDEMpy until no discharge was detected for at least 1 s. The final particles positions were then exported and projected onto a 2D plane, allowing the sAoR to be calculated as the slope of the best linear fit—minimising the root-mean-square-error—of the material surface, ensuring consistency with the experimental analysis.

3.3. Rotating drum simulations

The rotating drum (Fig. 6) was modelled at true scale. The cylindrical outer wall (drum) is made of stainless steel, and the front and back plate of glass. A time step analysis and a sensitivity analysis were performed (Appendix B), and the simulation-specific parameter settings are shown in Table 7.

Table 6
Hertz–Mindlin parameter space for ledge test calibration of rolling and static particle–particle friction.

Parameter		Levels	Value
$NaBH_4$-$NaBH_4$	μ_s	5	[0.05, 0.275, 0.5, 0.725, 0.95]
	μ_r	5	[0.001, 0.23825, 0.4755, 0.71275, 0.95]
	e	1	0.5
$NaBH_4$-Wood	μ_s	1	0.25
	μ_r	1	0.01
	e	1	0.5

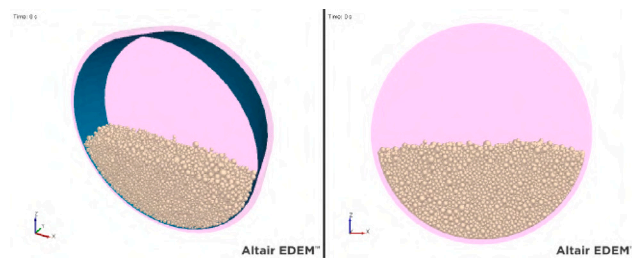

Fig. 6. Simulation setup of the rotating drum test. The drum (84 mm in diameter and 20 mm wide) is made of stainless steel, with glass front and back plates. The setup is filled with 27.5 g of granular $NaBH_4$. The particle size distribution of Fig. 2 is reproduced by scaling the spherical base particle (diameter 1.862 mm) according to the scaling factors and associated mass fractions presented in Table 4.

In contrast to the ledge test, which is inherently transient, the rotating drum reaches steady-state operation in which the free-surface slope fluctuates in time but remains bounded around an equilibrium value. Consequently, variations in the initial state become irrelevant for sufficiently long rotation times, allowing the number of repetitions to be reduced to one instead of the three typically required. A single particle bed was therefore generated and reused for all simulations.

Table 8 shows the rotational speeds and the interaction parameters for the design of experiments. Five levels were used for the particle–particle friction coefficients, and combined with the three rotational speeds this resulted in 75 unique simulations. Particle–wall interactions for the glass plates were fixed at 0.5 (μ_s) and 0.001 (μ_r) based on the sensitivity analysis. The particle–wall interactions for the steel drum were adopted from [25].

Each simulation was run for 21 s, consisting of 1 s settling time following by 20 s of rotation. A post-processing script provided by Granutools [26] was used to analyse the simulation results and extract the cohesive index, ensuring consistency with the experimental analysis.

3.4. Inclined surface test simulations

Fig. 7 shows the inclined surface test simulation setup, modelled at true scale. A time step analysis was performed with two time steps: 40% (as used for the ledge test) and 60% (as used for the rotating drum) of the Rayleigh time steps (T_R), and the results are provided in Appendix C. The simulation was run three times for 30 s. The simulation-specific parameter settings are summarised in Table 9, and the interaction parameters are given in Table 10.

The particle–wall static friction coefficients for the stainless steel, perspex, and aluminium walls were adopted from our previous work [8], in which the wall friction coefficient was measured using wall-friction ring shear tests. The particle–wall rolling friction coefficient

Table 7
Rotating drum simulations settings.

Parameter	Unit	Value
Factory Type	–	Dynamic
Total Mass	g	27.5
Generation Rate	g/s	27.5
Generation Time[a]	s	1
Settling Time[b]	s	1
Simulation Time	s	21
Time step[c]	% of T_R	60
	s	4.97e−06

[a] To reduce computational time, a particle bed is generated once, and used for each simulation.
[b] Each simulation has different rolling and friction coefficients, hence the particle bed is allowed to settle for 1 s before rotation is initiated.
[c] Time step analyses can be found in Appendix B.

Table 8
Hertz–Mindlin parameter space for rotating drum calibration of rolling and static particle–particle friction. A sensitivity analysis illustrating that $\mu_{r,\mathrm{NaBH_4-NaBH_4}}$ and $\mu_{s,\mathrm{NaBH_4-NaBH_4}}$ affect the dAoR most can be found in Appendix B.

Parameter		Levels	Value
Rotational Speed		3	[1,10,60] rpm
$NaBH_4$-$NaBH_4$	μ_s	5	[0.001, 0.23825, 0.4755, 0.71275, 0.95]
	μ_r	5	[0.05, 0.275, 0.5, 0.725, 0.95]
	e	1	0.5
$NaBH_4$-Glass	μ_s	1	0.5
	μ_r	1	0.001
	e	1	0.5
$NaBH_4$-Drum	μ_s	1	1
	μ_r	1	1
	e	1	0.5

Table 9
Inclined surface test simulations settings.

Parameter	Unit	Value
Factory Type	–	Dynamic
Total Mass	kg	0.5
Generation Rate	kg/s	1.0
Generation Time	s	0.5
Settling Time[a]	s	1.5
Settling Time[b]	s	2
Tilting Rate	°/s	1.9
Tilting Time	s	21
Simulation Time	s	30
Time step[c]	% of T_R	60
	s	4.97e−06

[a] Settling time after particles have been generated.
[b] Settling time after aluminium hatch has been lifted upwards.
[c] Time step analyses can be found in Appendix C.

Table 10
Hertz–Mindlin parameters for inclined surface test validation of rolling and static particle–particle friction.

Parameter		Value
$NaBH_4$-$NaBH_4$	μ_s	0.643
	μ_r	0.284
	e	0.5
$NaBH_4$-Stainless Steel	μ_s	0.247
	μ_r	0.3
	e	0.5
$NaBH_4$-Aluminium	μ_s	0.295
	μ_r	0.01
	e	0.5
$NaBH_4$-Perspex	μ_s	0.364
	μ_r	0.01
	e	0.5

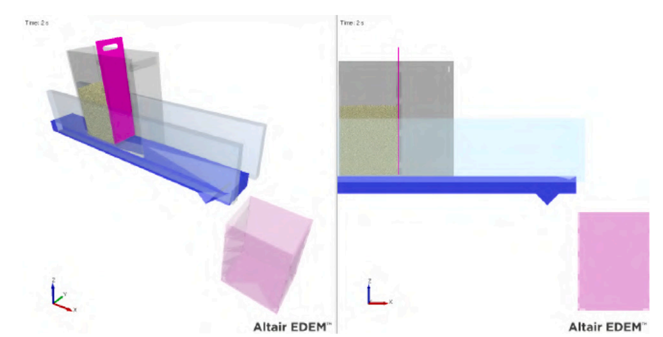

Fig. 7. Simulation setup of the inclined surface test, consisting of a top bin, a flat surface with side walls, and receiving bin. The stainless steel surface (bottom plate, highlighted in blue), including the side walls and top bin, rotates about a pivot located at the outermost point of the triangular support beneath the bottom plate. The bottom plate is made of stainless steel, while all other walls are made of perspex, except for the aluminium hatch in the top bin. The setup is filled with 500 g of granular $NaBH_4$. The particle size distribution of Fig. 2 is reproduced by scaling the spherical base particle (diameter 1.862 mm) according to the scaling factors and associated mass fractions presented in Table 4.

was left unchanged at 0.01 (the default value in EDEM) for all walls. The only exception was the stainless steel surface, where it was slightly increased to 0.3, within the same order of magnitude as the particle–particle rolling friction. This adjustment did not significantly affect heap formation after opening the hatch, nor the associated Ψ_1, but prevented a small number of particles from slowly rolling into the discharge bin immediately after.

Simulations are post-processed using EDEMpy using a procedure similar to that used for the ledge test simulations, such that Ψ_1 and Ψ_3 can be determined as the slope of the best linear fit to the material–air surface.

4. Results

This section presents the results of the calibration, verification, and validation of coefficients of static and rolling friction for particle–particle interactions of free-flowing $NaBH_4$ in the dense flow regime. Note that the term ‘verification’ is used in the same sense as applied by Hadi et al. [27], referring to the re-evaluation of a calibrated parameter set to confirm its accuracy—especially since the parameters are derived through interpolation between 25 simulated μ_s–μ_r combinations.

4.1. Calibration

Fig. 8 presents the mean sAoR obtained from the ledge test simulations as a function of μ_s and μ_r. The experimental results, including its 95% confidence interval, are shown for comparison and to identify parameter combinations that reproduce sAoR values consistent with the measurements.

Fig. 9 presents the cohesive index, obtained from the rotating drum simulations at three rotational speeds, as a function of μ_s and μ_r. The experimental mean and 95% confidence interval are shown to enable comparison with the simulation results. To identify a calibrated parameter set, the results from both the ledge test and rotating drum

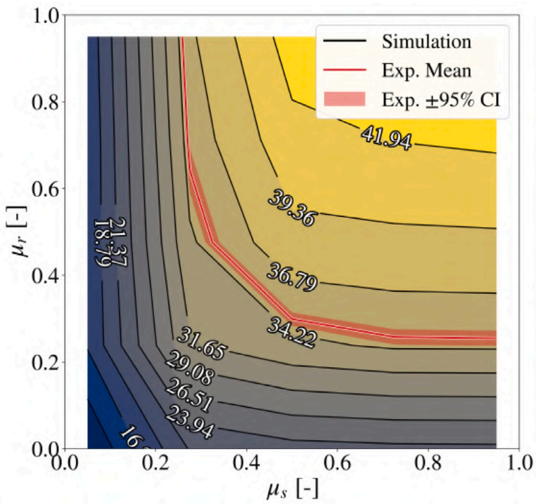

Fig. 8. Contourplot of the mean sAoR obtained from the ledge test simulations. The experimental results of [8] are shown with mean value and 95% confidence interval. Simulation confidence intervals were found to be small relative to parameter-induced variation and are therefore not shown for clarity.

are combined. Parameter combinations that reproduce the experimental results within the 95% confidence intervals are extracted from the contourplots and shown in Fig. 10. This is done for all KPIs, and their intersections define the regions of the parameter space that simultaneously satisfy the experimental constraints.

Two of these regions are identified where all KPIs—except those at 10 rpm—are reproduced. These regions are indicated in black in Fig. 10. The midpoints of these regions are selected as representative calibrated parameter sets, yielding $[\mu_s, \mu_r] = [0.429, 0.367]$ and $[0.643, 0.284]$, as also highlighted in Fig. 10.

The cohesive index of the rotating drum at 10 rpm is not reproduced by the calibrated parameter sets. This deviation may be attributed to the evolving flow dynamics for rotating drums at intermittent rotational speeds, which will be further discussed in Section 5.

4.2. Verification

The calibrated parameter sets were derived through interpolation of the 25 simulated μ_s–μ_r combinations. To verify their accuracy, both the ledge test and the rotating drum were repeated using the two calibrated sets. Similar to the calibration process, the ledge test is simulated three times, and the rotating drum only once for each rotational speed.

Table 11 presents the verification results, including the mean sAoR and its confidence interval, as well as the cohesive index, alongside the corresponding experimental data.

During calibration, only the mean simulation results were used to identify candidate parameter sets, in order to efficiently explore the parameter space. In contrast, the verification step evaluates the agreement between simulations and experiments, and therefore incorporates confidence intervals where available.

The results indicate that only one of the two parameter sets satisfies the verification criterion of Fig. 4, i.e. that the simulation results fall within or (where applicable) overlap with the experimental 95% confidence intervals. The deviation of the second parameter set may be attributed to the relatively coarse parameter space, as this set lies further from the originally simulated μ_s–μ_r combinations.

Based on these findings, the verified parameter is identified as $[\mu_s, \mu_r] = [0.643, 0.284]$.

4.3. Validation

To validate the predictive performance of the verified friction parameters, the inclined surface test (unseen during calibration) was simulated three times for both the slow ($0.556°/s$) and fast ($1.9°/s$) tilting rates. The simulation results for Ψ_1 and Ψ_3 are presented in Table 12 alongside their experimental counterparts.

Table 11
Verification results for the ledge test and rotating drum simulations using the calibrated parameter sets, compared with their experimental counterparts. Agreement is assessed based on the 95% confidence intervals, i.e. whether the simulation results fall within, or (where applicable) overlap with, the experimental intervals.

KPI		Experiments	Simulations - $[\mu_s, \mu_r]$	
			$[0.429, 0.367]$	$[0.643, 0.284]$
sAoR [°]		34.93 ± 0.31	36.12 ± 0.65	35.44 ± 0.21
CoI	1 rpm	12.13 ± 1.3	12.06	12.62
	60 rpm	8.77 ± 0.35	9.70	8.37

Table 12
Validation results for the inclined surface test simulations using the verified parameter set, compared with their experimental counterparts, showing mean angles with 95% confidence intervals. Ψ_1 and Ψ_3 are determined similar to the experimental procedure (for more details the reader is referred to the dataset [12]). Validation of requires a relative error of less than 5%.

	KPI	Experiments	Simulations
Slow Rate	Ψ_1[°]	29.15 ± 0.56	28.30 ± 0.04
	Ψ_3[°]	35.29 ± 3.44	36.49 ± 0.17
Fast Rate	Ψ_1[°]	29.06 ± 0.38	28.36 ± 0.25
	Ψ_3[°]	30.54 ± 1.50	35.61 ± 0.67

The results show that both angles are captured accurately for the slow tilting rate, with relative errors of 2.9% for Ψ_1 and 3.4% for Ψ_3 (for the latter, the experimental confidence interval fully encompasses the simulation interval). For the fast tilting rate, Ψ_1 is also reproduced accurately (2.4% error), while the slope in the discharge bin (Ψ_3) cannot be captured within the predefined 5% tolerance. Even when accounting for confidence intervals a relative error of 9.1% remains.

These results indicate a reduction in predictive accuracy for the fast tilting rate. This is expected, as the inclined surface test becomes more sensitive to particle–wall interactions at the stainless steel surface for more dynamic flow conditions, while these parameters were not included in the calibration and verification steps. Nevertheless, the observed deviation (when accounting for confidence intervals) remains within the 5%–10% range commonly adopted in DEM studies and is therefore considered acceptable.

Accordingly, the particle–particle friction parameters are considered validated as $[\mu_s, \mu_r] = [0.643, 0.284]$.

5. Discussion

Three test setups were used to derive the inter-particle friction parameters for free-flowing $NaBH_4$, following the calibration–verification–validation methodology described in Fig. 4. This framework ensured that the parameters were calibrated against multiple flow configurations using ledge tests and rotating drum tests, verified to correct for interpolation errors, and validated using an inclined surface test that was not part of the calibration procedure.

The aims of this study were to model the flow behaviour of $NaBH_4$ in the dense flow regime, and to examine the use of the inertial number for granular flow classification. Therefore this section analyse the flow profiles of the setups to first verify that they indeed represent dense-flow conditions, but also to highlight the spatial dependency of the inertial number. We then discuss the diverging simulation results for the 10 rpm rotational speed of the rotating drum tests, and the validation simulations are examined in more detail. Finally, the influence of out-of-plane thickness and boundary conditions across the three setups is addressed.

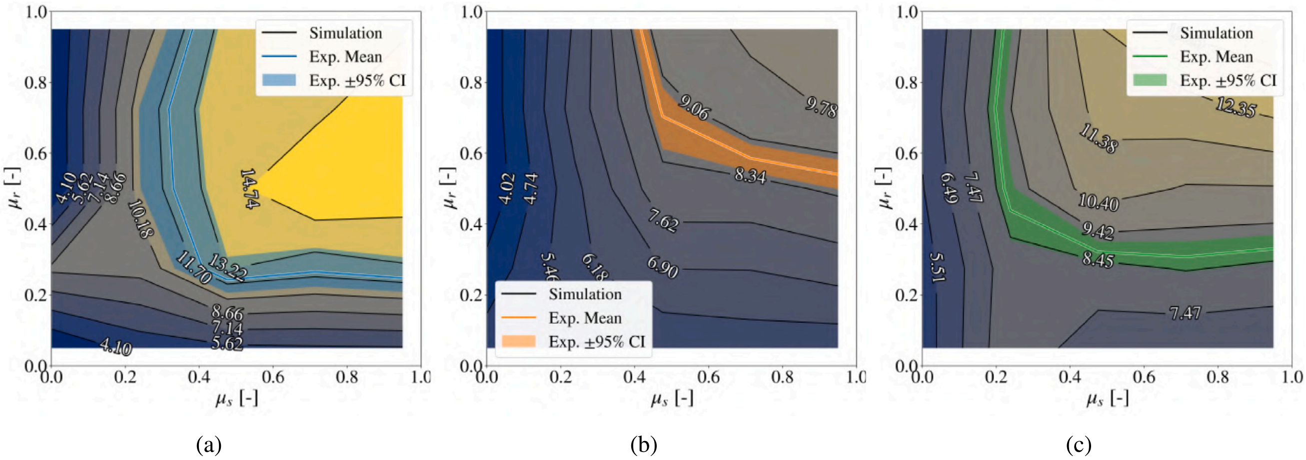

Fig. 9. Contourplots of the cohesive index obtained from the rotating drum simulations at three rotational speeds with (a) 1 rpm, (b) 10 rpm, and (c) 60 rpm. The experimental results of [8] are shown with mean value and 95% confidence interval.

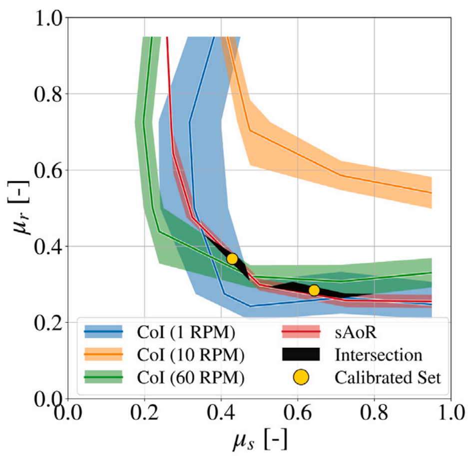

Fig. 10. Intersection plot for the static angle of repose and cohesive index. The coloured areas represent the μ_s–μ_r combinations that successfully satisfy the experimental constraints. Their intersections, highlighted in black, define candidate parameter sets that satisfy all constraints, except for the rotating drum at 10 rpm. The midpoint of both areas are selected as representative calibrated parameter sets.

5.1. Flow regimes and inertial numbers

Granular flow is commonly classified into three regimes [28]: quasi-static, dense, and gaseous, and to determine the flow regime for each setup, the inertial number I is required [9,19]. As we expect the dense flow regime to prevail in the setups used for this study, the inertial number is computed using the formulation for free-surface flows [9]:

$$I = \frac{5}{2}\frac{\bar{V}d}{h\sqrt{ghcos(\theta)}} \tag{14}$$

where d is the particle diameter [m], $\bar{V}$ the mean flow speed [m/s], h the layer thickness [m], and θ the inclination of the flowing layer. Typically, values of $I < 10^{-3}$ correspond to the quasi-static flow regime, values of $I > 0.3$ indicate the gaseous flow regime, and intermediate values reflect the dense flow regime.

The inclined surface test lies between the ledge test and rotating drum (60 rpm) in terms of static and dynamic flow behaviour, thus demonstrating dense-flow behaviour in the latter two setups justifies assigning the inclined surface test to the dense flow regime. Therefore, the simulation results of the inclined surface test are not discussed further in this section.

The values of $\bar{V}$, h, and θ can be directly derived from the simulation data once the flowing layer is identified. For the ledge test, the distinction between static and flowing particles is well defined, but for the rotating drum this distinction is less clear due to the dynamic nature of the setup. Therefore, we adopted a velocity-based approach. At each time step, the velocity of all the particles in the setup is computed, and the flowing layer is defined using minimum and maximum normalised velocity thresholds. This results in numerous candidate flowing layers, and for each of them we compute $\bar{V}$, h, θ, and the corresponding I.

First, the analysis (described in detail in Appendix D) is used to examine the structure and evolution of the flowing layer, which is illustrated through quiver plots. In the ledge test (Fig. 11), the flow begins as a relatively thick layer near the hatch opening (0.2 s), and progressively thins as particles flow downwards (1.0 s and 1.6 s). The velocity gradient of the flowing layer is most pronounced directly after the hatch opens, and gradually weakens as the particles decelerate.

In the rotating drum simulations (Fig. 12), the flowing layer forms along the free surface. At 1 rpm, the layer thickness fluctuates strongly due to discrete avalanching behaviour. At 60 rpm, the layer becomes thicker and more continuous, with the highest velocities concentrated near the free surface. These observations illustrate that the dynamics of the flowing layer are setup-dependent and exhibit either continuous or discontinuous behaviour.

Second, the analysis yields a family of layer thicknesses h and inertial numbers I as a function of normalised velocity and time. Fig. 13 shows the temporal evolution of the inertial number I together with the corresponding layer thicknesses for both simulation setups. For a broad normalised-velocity interval (0.1–1.0), both the ledge test and rotating drum at 60 rpm exhibit dense-flow behaviour ($10^{-3} < I < 0.3$). In contrast, narrower velocity intervals reveal a fast-moving transition towards the gaseous regime, while the slowest layers remain in the dense flow regime.

Furthermore, the increase of inertial number with normalised velocity thresholds is accompanied by a progressive reduction in the flowing layer. In the ledge test, this effect causes some of the higher-velocity layers to become too thin for a reliable estimation of I, resulting in missing values at later time steps. For the rotating drum tests, the layer thickness varies over time, oscillating around a mean value, reflecting the periodic nature of the flow.

These findings confirm that the setups used in this study exhibit predominantly dense-flow behaviour when considering the bulk of the flowing layer. However, a key observation is that the inertial number strongly depends on how the flowing layer is defined.

For broader normalised-velocity-thresholds, the flow is consistently classified as dense, whereas narrower thresholds isolate thin, fast moving particle layers near the surface that exhibit slightly higher inertial

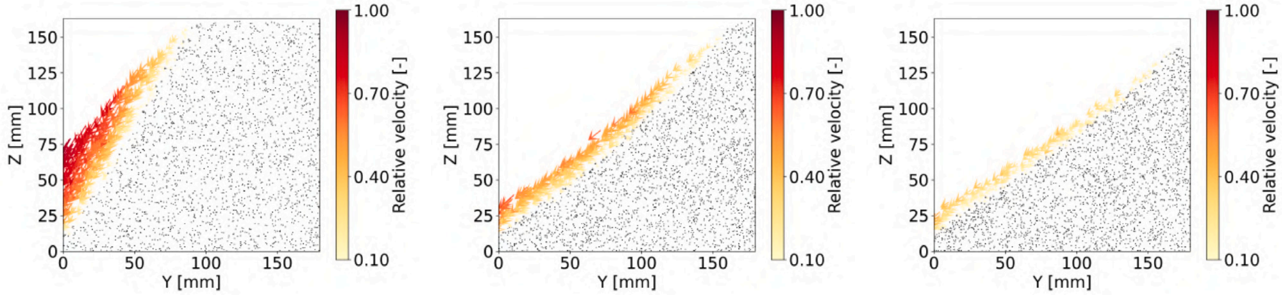

(a) (b) (c)

Fig. 11. Quiver plots for ledge test simulations after opening the hatch for (a) 0.2 s, (b) 1 s, and (c) 1.6 s. Particles not meeting the minimum velocity are depicted in black.

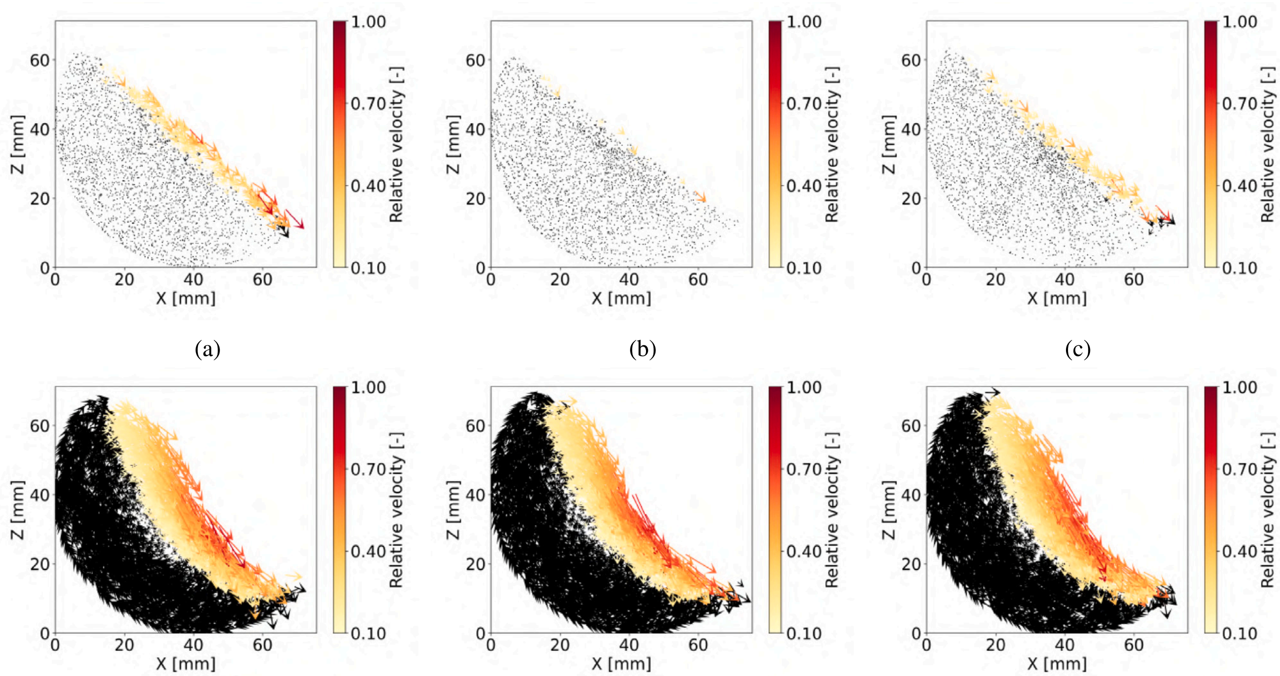

(a) (b) (c)

(d) (e) (f)

Fig. 12. Quiver plots for rotating drum simulations for (a, b, c) 10 s, 15 s, and 20 s rotation at 1 rpm, and (d, e, f) 10 s, 15 s, and 20 s rotation at 60 rpm. Particles not meeting the minimum normalised velocity are depicted in black.

numbers associated with gaseous flow. This demonstrates that multiple flow regimes can coexist within a single configuration, depending on the velocity thresholds used to define the flowing layer. As these thresholds correspond to specific spatial regions within the bulk, the inertial number is inherently spatially dependent.

Physically this reflects the stratified nature of free-surface granular flows. Near the free surface, particles move rapidly, and experience frequent collisions and brief loss of contact, resulting in high inertial numbers. In contrast, deeper in the material bed, particles move more slowly, remain in contact, and maintain force networks to transmit the confining stresses, resulting lower inertial numbers.

As the high-velocity surface layers are relatively thin, the overall flow behaviour remains dominated by dense flow, even though localised gaseous behaviour occurs within the same system. This highlights that a single inertial number cannot fully describe free-surface flows, as it is inherently spatially dependent and strongly affected by the definition of the flowing layer.

5.2. *Rotating drum tests*

The slight deviation observed in Fig. 10 for the rotating drum simulations at 10 rpm suggests that this rotational speed cannot be reliably used for calibration and verification. This deviation can be attributed to the well-known transition behaviour in rotating drums [29], and in this case from the rolling regime to the cascading regime.

In the rolling regime, the particle bed largely moves as a solid body, with flow occurring through discrete avalanching (stick–slip behaviour). In contrast, the cascading regime is characterised by a continuous flowing layer on top of a more slowly moving bulk, with particle typically following curved trajectories. Granular flows in a

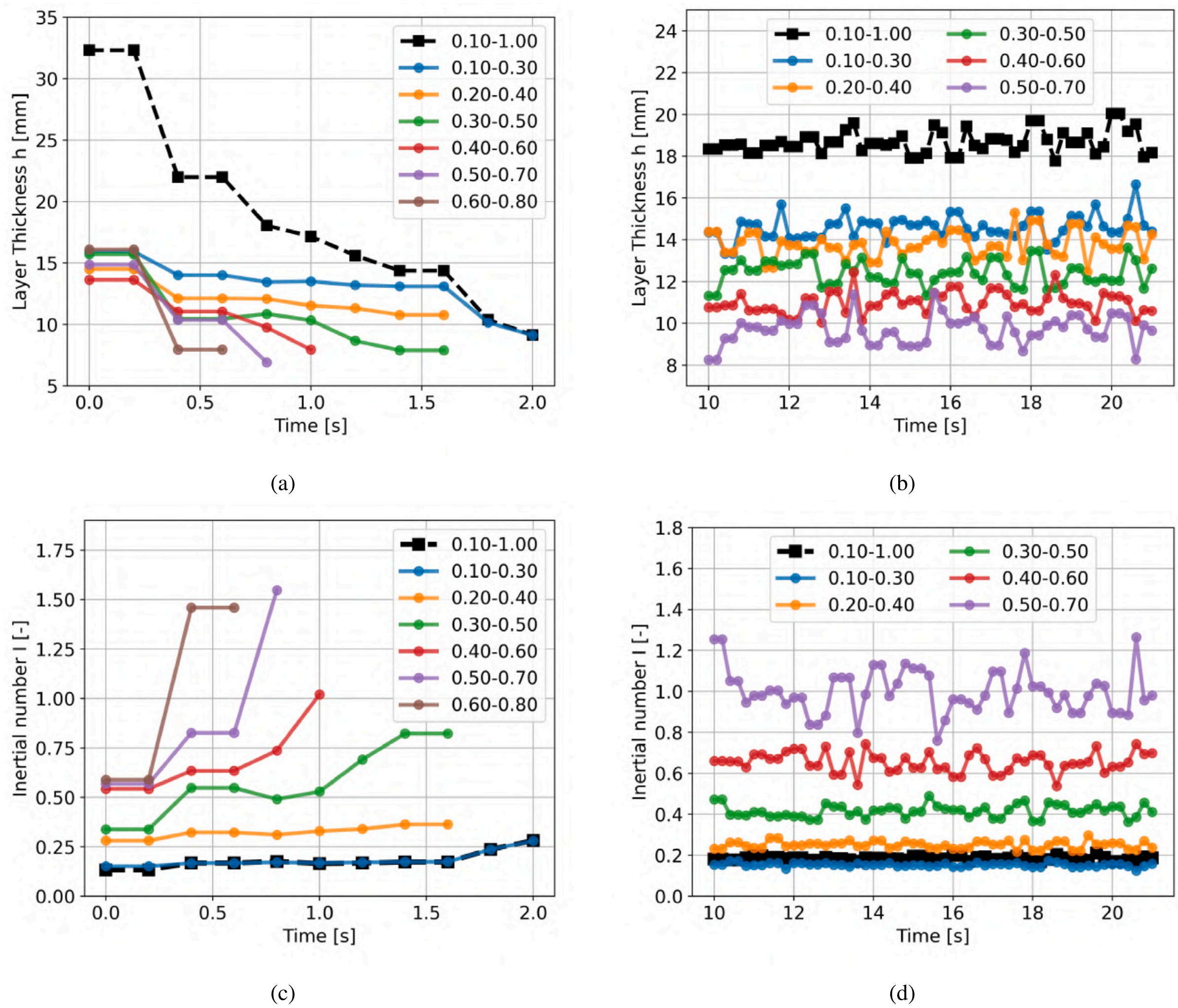

Fig. 13. Comparison of (a,b) layer thicknesses and (c,d) inertial numbers for the ledge test and rotating drum (60 rpm) simulations For the ledge test the first two seconds of discharge are most relevant for the analysis, and for the rotating drum simulations data are recorded from $t = 10$ to $t = 20$. The legend lists the normalised velocities intervals used to define the flowing layer. Each interval is used to estimate h and I and corresponds to one coloured curve.

transitional state between these regimes may exhibit characteristics of both.

To understand this, we first consider the parameters governing the rotating drum setup. While the inertial number describes the flow behaviour of the flowing particle layer (as dense flow), the Froude number (Fr) characterises the drum as a whole, accounting for both the rotating speed and the drum diameter [25,29]:

$$Fr = \sqrt{\frac{\omega^2 D}{2g}} \tag{15}$$

where D is the drum diameter, ω the rotational speed, and g the gravitational acceleration. For a rotating drum with $D = 84$ mm, and a rotational speed range of 1-60 rpm, the Froude number spans:

$$6.9 \cdot 10^{-3} \leq Fr \leq 4.1 \cdot 10^{-1} \tag{16}$$

According to Mellmann [29], this range includes slumping, rolling, and cascading regimes. Notably, these Froude number-defined regimes describe the global flow behaviour of the drum, while the inertial number solely describes the behaviour of the flowing layer at the free surface. As a result, a drum operating in a given regime (for example cascading) may still exhibit quasi-static, dense, or gaseous flow, depending on the spatial region considered.

Santos et al. [30] investigated the critical Froude number (Fr_c) for the rolling–cascading transition. They present two equations: the original equation dated from 1996, and a modified version incorporating particle sphericity (Eq. (17)), which improved predictive accuracy:

$$Fr_c = \frac{2 d_v \phi}{D} \tag{17}$$

where d_v is the volume-equivalent diameter, ϕ the sphericity, and D the drum diameter. Combining Eq. (15) with Eq. (17) yields an expression for the critical rotational speed for the rotating drum:

$$\omega_c = \sqrt{\frac{8g}{D^3} d_v \phi} \tag{18}$$

Using $d_v = 1.8$ mm (the arithmetic mean of the PSD of Fig. 2), and $\phi = 0.85$ (the circularity of the granules [8]), the critical rotating speed is approximately 0.56 rad/s (≈5 rpm). This aligns with experimental observations in [8], where the transition becomes noticeable around 10 rpm and the S-shape of the flowing layer becomes more pronounced. For simulations, where $\phi = 1$, the critical speed increases slightly to 6.25 rpm.

Consequently, the rotating drum operates in the rolling regime at 1 rpm, the cascading regime at 60 rpm, and are in a transitional state at 10 rpm.

In summary, the simulation results successfully reproduce fully developed rolling (1 rpm) and cascading (60 rpm) regimes using spherical particles. However, at 10 rpm the system operates in a transitional state, where the flow behaviour becomes more complex than can be captured by a single KPI, such as the cohesive index. This limitation primarily affects the intermediate state and does not compromise the accuracy of the model for well-developed Froude-number-defined flow regimes. Nevertheless, it highlights the need for future work to improve the modelling of transitional behaviour, for example by incorporating particle shape effects or more advanced contact models.

5.3. Inclined surface tests

Within the calibration–verification–validation framework used in this study, inter-particle friction parameters can be calibrated and verified independently before particle–wall interactions are introduced in the validation step. The particle–wall parameters required for the latter are partly derived from quasi-static wall friction tests, and partly retained at their default values. However, these quasi-static measurements may not fully represent particle–wall interactions under dynamic, dense flow conditions. In the inclined surface test, particle–wall friction becomes increasingly relevant at higher tilting rates. As a result, deviations are observed in Ψ_3, which is measured after discharge of the material. In addition, the experiments exhibit distinct discrete avalanching, whereas the simulations showed this to a much lesser extent.

These observation indicate that dynamic wall effects are not fully captured. In practice, inclined surface tests are commonly used to estimate the effective wall friction coefficient from the maximum inclination angle $\Psi_{\max}$, using $\mu_s = \tan(\Psi_{\max})$. For the experiments presented in here, this yields $\mu_s \approx \tan(35°) \approx 0.7$ for the stainless steel surface, which is considerably higher than the quasi-static value used in the simulations. Exploratory simulations using this value showed improved agreement with the observed discharge behaviour, suggesting that wall-friction parameters may be flow-regime dependent.

A logical extension for future work is therefore to treat the particle–wall friction in the inclined surface test as a secondary calibration step, using additional KPIs sensitive to wall interactions, such as discharge time, flow-velocity gradients, or heap geometry. This would naturally require an additional validation step using a representative setup, as the inclined surface test would then no longer serve as an independent validation case.

5.4. Thickness and boundary conditions

The three setups used for the calibration–verification–validation differ in their out-of-plane thickness and boundary conditions, which may influence the results. This section briefly assesses their impact.

For the ledge test, the experimental setup has a width-to-diameter ratio (out-of-plane-thickness in terms of particle diameters) greater than 50, ensuring negligible side-wall effects [31]. In the DEM simulations, periodic boundaries were used to reduce computational costs, resulting in a width-to-diameter ratio of 10. As shown in Appendix A, this does not significantly affect results.

The rotating drum has a relatively small width (20 mm, approximately eleven particle diameters), which may introduce minor side-wall effects. However, these are expected to be limited due to the dynamic nature of the flow and the low friction glass walls. In the simulations, particle–wall friction for the glass walls was set to zero to minimise confinement effects.

For the inclined surface test, the experimental setup has a width-to-diameter ratio of approximately 40, which sufficiently limits wall effects. This geometry was replicated one-to-one in the DEM simulations where particle–wall interactions are explicitly included.

Overall, the three setups differ in out-of-plane thickness and boundary conditions, which may influence setup-specific flow behaviour. However, in each case, the simulation setups closely follows the experiments, or it has been shown that simplifications do not significantly affect the results.

Despite these differences, the validated parameter set consistently reproduces the relevant bulk flow behaviour across all configurations. This indicates that the particle–particle static and rolling friction coefficients are robust with respect to variations in boundary conditions and that this is not limited to a single type of confinement.

6. Conclusion

This study aimed to model the free-flowing behaviour of granular $NaBH_4$ within the dense flow regime using the Discrete Element Method. The inter-particle friction coefficients (μ_s and μ_r) were calibrated using two setups: a ledge test (static) and a rotating drum test (dynamic), considering rotational speeds of 1, 10, and 60 rpm. Two parameter sets were identified that successfully reproduced the static angle of repose and the cohesive indices at 1 and 60 rpm. Verification showed that one of the sets provided sufficiently accurate results and was subsequently selected for validation.

The predictive capability of this parameter set was assessed using an inclined surface test, which was not part of the calibration process, yielding results in good agreement with experiments. The analysis of the flowing layer characteristics and the computed inertial numbers for free-surface flows confirmed that the investigated flows satisfy the criteria for the dense flow regime.

Overall, the validated friction parameters enable consistent reproduction of static and dynamic flow behaviour of free-flowing $NaBH_4$ under the laboratory conditions considered. The results further demonstrate that spherical particles with rolling resistance, using the Hertz–Mindlin and Rolling Model C contact models, can reasonably approximate the dense granular flow of $NaBH_4$ in well-developed rolling and cascading regimes. However, discrepancies observed in the transitional state (e.g. at 10 rpm) indicate that this approach has limitations when the flow behaviour becomes more complex.

The validated parameter set therefore provides a useful basis for DEM simulations of $NaBH_4$ under dry, dense-flow conditions at the laboratory scale. This supports initial modelling of storage and handling processes relevant to the use of $NaBH_4$ as an alternative fuel in maritime applications. However, further work is required to assess transferability to industrial-scale systems, where additional factors such as particle shape, particle–wall interactions, scale effects, and time-dependent consolidation may influence flow behaviour.

Future work

While the results are promising, several directions for future work remain to extend the applicability of the model. First, particle–wall interactions were not explicitly calibrated in this study, yet were shown to influence flow behaviour. Further work should therefore focus on their independent experimental characterisation and incorporation into the calibration framework.

Second, the suitability of the dynamic angle of repose as a KPI in rotating drums requires further investigation. Alternative approaches, such as using the full free-surface profile, as explored in previous work, may improve robustness.

Third, while spherical particles are successfully used in this study, incorporating particle shape in future DEM models is recommended for more complex flows, as indicated by the rotating drum at 10 rpm. In addition, scaling up from laboratory to industrial scale remains an important step to assess transferability of the validated parameters.

Finally, the present work shows that the inertial numbers should be interpreted as a spatially dependent quantity. Further investigation of the proposed velocity-threshold analysis is therefore advised, along with extending the calibration–verification–validation analysis to non-dense regimes and incorporating time consolidation effects relevant for storage and handling applications.

Table A.1
Ledge test simulations settings, including scaled setups.

Parameter	Unit	Value			
Width/D_{50}	–	66 (full scale)	30	20	10
Factory Type	–	Dynamic	Dynamic	Dynamic	Dynamic
Total Mass	kg	1.90	0.886	0.578	0.289
Generation Rate	kg/s	2.00	0.993	0.609	0.304
Generation Time[a]	s	1	1	1	1
Settling Time[b]	s	1	1	1	1
Simulation Time[c]	s	Variable	Variable	Variable	Variable

[a] Particles are generated for each simulation in approximately 1 s.
[b] The hatch of the ledge box rapidly opens after 2 s, allowing the particles to settle.
[c] EDEMpy is used to run the simulations as long as required (ranging from <10 to >20 s), to ensure a stable material bed for at least 1 s before stopping.

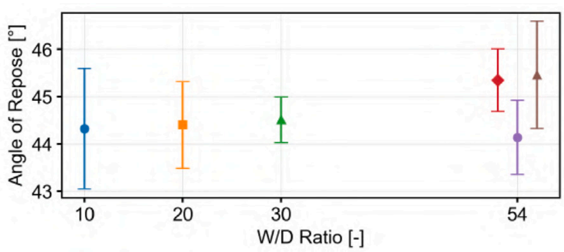

Fig. A.1. Scaling of the ledge test simulations for width-to-diameter (W/D) ratios. Time step = 40% of T_R, N = 3. At W/D = 54, the purple errorbar represents the centre of the setup, and the red and brown errorbar both sides near the walls.

CRediT authorship contribution statement

M.C. van Benten: Writing – original draft, Methodology, Formal analysis, Data curation, Conceptualization. **J.T. Padding:** Writing – review & editing, Supervision, Funding acquisition. **D.L. Schott:** Writing – review & editing, Supervision, Funding acquisition.

Declaration of competing interest

The authors declare that they have no known competing financial interests or personal relationships that could have appeared to influence the work reported in this paper.

Acknowledgements

This work is part of the project SH2IPDRIVE with project number MOB21013, funded by the Ministry of Economic Affairs and Climate Policy, RDM regulation, carried out by the Netherlands Enterprise Agency.

Appendix A. Ledge test scaling, stability, and sensitivity analysis

Table A.1 shows the ledge test simulation settings used for the scaling and time stability analysis. The total mass of $NaBH_4$ was adjusted to maintain a consistent filling height across all the simulations, and the generation rate was scaled to achieve comparable filling times. The corresponding scaling and time stability results are shown in Fig. A.1 and Fig. A.2, respectively. Additionally, a sensitivity analysis is shown in Fig. A.3.

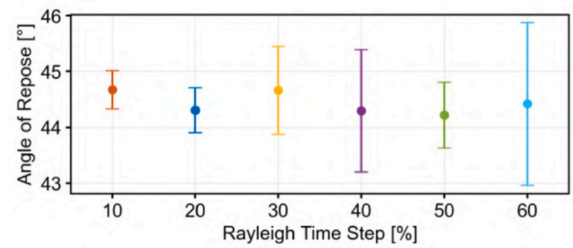

Fig. A.2. Time stability analysis of the ledge test simulations. W/D = 10, N = 3.

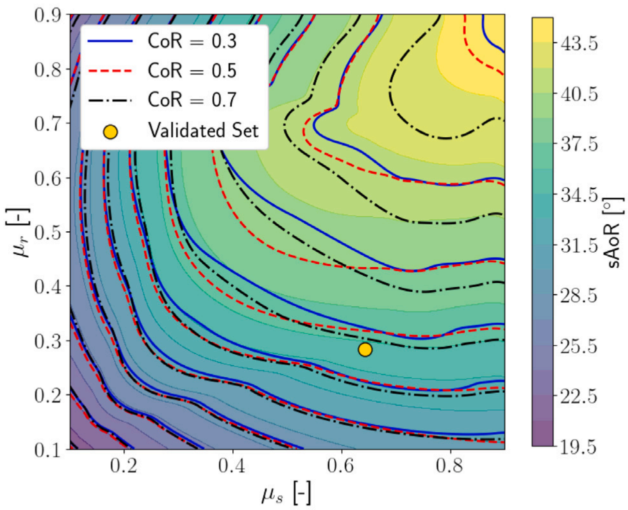

Fig. A.3. Sensitivity analysis of the ledge test setup. The static angle of repose (sAoR) is shown as a function of the coefficients of restitution (e), static friction (μ_s), and rolling friction (μ_r). The results demonstrate that variations in e have a limited influence on the sAoR compared to the friction parameters. This analysis was performed without a particle size distribution. G = 33 MPa, RYT = 20%, N = 1.

Appendix B. Rotating drum stability and sensitivity analysis

Fig. B.1 presents the time stability analysis for the 60 rpm rotating drum simulations, as this rotational speed represents the most dynamic scenario. The results show that time steps of 80%–100% of T_R produce large fluctuations in the kinetic energy. A time step of 70% of T_R is therefore the upper limit for stable simulations. To be conservative, we selected a time step of 60% of T_R.

Using this stable time step, a Plackett–Burman sensitivity analysis was performed to assess the effect of the coefficient of restitution e, static friction μ_s, and rolling friction μ_r of both particle–particle and particle–wall interactions on the dynamic angle of repose (dAoR) and the cohesive index (CoI). The parameters levels used in the analysis are listed in Table B.1, and the corresponding experimental matrix in Table B.2. Simulations were conducted for both low (1 rpm) and high (60 rpm) rotational speeds. The results, shown in Fig. B.2, indicate that particle–particle interaction dominate the particle–wall interactions in all cases. At both rotational speeds, inter-particle rolling friction μ_r has the largest influence on both dAoR and CoI, followed by the static friction μ_s for three out of four scenarios. These findings justify the selection of the particle–particle μ_r and μ_s parameters for calibration.

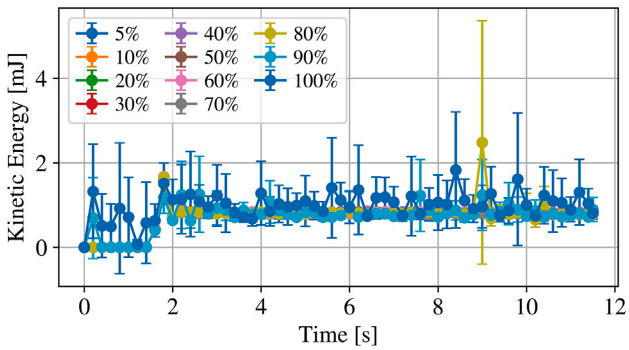

(a)

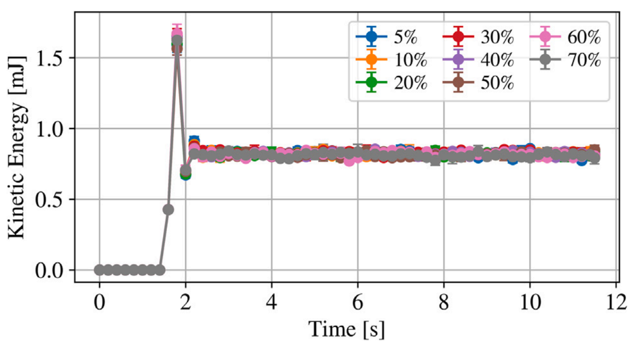

(b)

Fig. B.1. Time stability analysis of the 60 rpm rotation drum simulations with (a) time steps up to 100% of T_R, and (b) time steps up to 70% of T_R. N = 3. (Rayleigh time step is here abbreviated as RYT.)

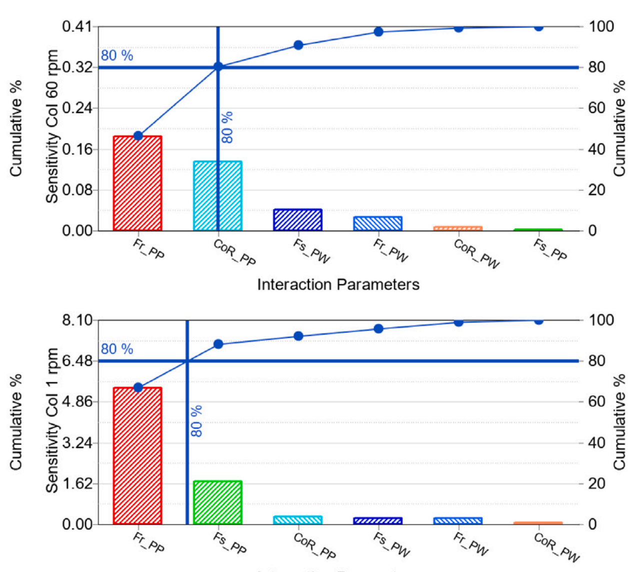

Fig. B.2. Pareto plots of the sensitivity of the cohesive index to the rotating drum interaction parameters at different rotational speeds. Altair Hyperstudy was used to run the Plackett–Burman sensitivity study defined by Tables B.1 and B.2. The horizontal and vertical lines show the thresholds for 80% of the contributions. For both 1 rpm and 60 rpm, the particle–particle rolling friction is the most influential parameter. At 1 rpm, static friction is the second most influential, while at 60 rpm the coefficient of restitution becomes more influential than the static friction. This suggests that the influence of e increases at higher rotational speeds. N = 1.

Table B.1
Parameter levels for rotating drum sensitivity analysis.

Parameter	$NaBH_4$ – Glass			$NaBH_4$ – $NaBH_4$		
	e	μ_r	μ_s	e	μ_r	μ_s
Level −1	0.25	0.001	0.25	0.25	0.001	0.25
Level 1	0.75	0.5	0.75	0.75	0.5	0.75

Table B.2
Plackett–Burman design of experiments for rotating drum sensitivity analysis for low (1 rpm) and high (60 rpm) rotational speeds.

Parameter	$NaBH_4$ – Glass			$NaBH_4$ – $NaBH_4$		
	e	μ_r	μ_s	e	μ_r	μ_s
Run 1	1	1	1	−1	1	−1
Run 2	−1	−1	1	1	1	1
Run 3	1	−1	−1	−1	1	1
Run 4	1	1	−1	1	−1	1
Run 5	1	−1	1	1	−1	−1
Run 6	−1	1	−1	1	1	−1
Run 7	−1	1	1	−1	−1	1
Run 8	−1	−1	−1	−1	−1	−1

Table C.1
Time stability analysis of the inclined surface test, including mean angles with 95% confidence intervals for two time steps. N=3. Note that the analysis was conducted using a slightly different parameter set than that used for final validation, resulting in a small offset in the absolute values of the angles.

Rayleigh time step	Angle 1 Ψ_1 [°]	Angle 3 Ψ_3 [°]
40%	27.77 ± 0.09	33.98 ± 0.16
60%	27.84 ± 0.29	34.31 ± 0.70

Appendix C. Inclined surface test stability analysis

For the time stability analysis of the inclined surface test simulations, Rayleigh time steps 40% (as used for the ledge test) and 60% (as used for the rotating drum test) were evaluated. Each simulation was repeated three times, and the effect of the time step on Ψ_1 and Ψ_3 is summarised in Table C.1. The results show that a Rayleigh time step of 60% can be used safely without compromising accuracy.

Appendix D. Procedure for inertial number estimation

Particle velocities were normalised by the maximum in-plane speed observed in the simulation, and an exhaustive set of virtually all plausible normalised velocity intervals was considered, ranging from narrow bands (e.g., 0.1–0.2 and 0.2–0.3) to broader intervals (e.g., 0.3–0.7, 0.4–0.9, and 0.1–1.0). For each interval, particles within the normalised speed range were treated as the flowing layer. For the rotating drum simulations, particles located too close to the drum wall, negative X-velocity, or positive Z-velocity were automatically excluded from the flowing layer.

The mean velocity $\bar{V}$ was then computed after projecting the 3D particle velocities on the relevant plane (YZ for the ledge test, XZ for the rotating drum test and the inclined surface test), and the inclination angle θ was assumed as the tangent of the two in-plane velocity components of $\bar{V}$.

The layer thickness h was estimated by discretising the flow layer into bins along the flow direction, calculating the maximum filling height of each bin, and averaging across bins. To reduce sensitivity to bin width, multiple bin widths were tested and the median layer thickness was used. This procedure was repeated for all velocity intervals and time steps, and is illustrated in simplified form in Algorithm 1 below. The full Python script is available in the dataset [12].

Algorithm 1: Identify Flowing Layer Data

Input:
Velocity intervals $[v_{\min}, v_{\max}]$ for normalised speed $(0 \le v_{\min} \le v_{\max} \le 1)$ (user-defined),
Bin sizes $\mathbf{B}$ (vector of x'-axis bin widths for thickness calculation)

Data:
Particle positions $\mathbf{P} \in \mathbb{R}^{N\times 3}$,
Particle velocities $\mathbf{V} \in \mathbb{R}^{N\times 3}$,
Particle masses $\mathbf{m} \in \mathbb{R}^{N}$,
Equipment positions $\mathbf{Q} \in \mathbb{R}^{M\times 3}$,
Drum radius $R_{\text{drum}} \in \mathbb{R}$

Result: $d,\ h,\ \bar{V},\ \theta$

for *each simulation* **do**
  for *each time step t* **do**
    Compute particle speeds:
    $\mathbf{v} = \|\mathbf{V}\| = \sqrt{V_x^2 + V_y^2 + V_z^2}$;
    Scale particle speeds:
    $\hat{\mathbf{v}} = \frac{\mathbf{v}}{\max(\mathbf{v})}$;
    For rotating drum; compute particle distance from centre (drum centre at $[0,0]$):
    $\mathbf{D} = \sqrt{P_x^2 + P_z^2}$;
    Identify flowing particles:
    $$\mathcal{F} = \begin{cases} \{i \mid v_{\min} \le \hat{\mathbf{v}}_i \le v_{\max} \wedge V_{i,x} \ge 0 \wedge V_{i,z} \le 0 \wedge \mathbf{D}_i < 0.95 R_{\text{drum}}\}, & \text{rotating drum} \\ \{i \mid v_{\min} \le \hat{\mathbf{v}}_i \le v_{\max} \wedge P_{i,x} > Q_{\text{ledge},x}\}, & \text{ledge test} \end{cases}$$
    Extract flowing layer data:
    $\mathbf{P}_{\mathcal{F}}, \mathbf{v}_{\mathcal{F}}$;
    Compute mean flow direction:
    $\mathbf{r} = \frac{1}{|\mathcal{F}|} \sum_{i\in\mathcal{F}} \mathbf{V}_{\mathcal{F},i}$;
    Normalise flow direction:
    $\hat{\mathbf{r}} = \frac{\mathbf{r}}{\|\mathbf{r}\|}$;
    Compute flow angle:
    $$\theta = \begin{cases} \operatorname{atan2}(\hat{r}_z,\ \hat{r}_y), & \text{ledge test} \\ \operatorname{atan2}(\hat{r}_z,\ \hat{r}_x), & \text{rotating drum} \end{cases}$$
    Rotate $\mathbf{P}_{\mathcal{F}}$ into flow-aligned frame:
    $\mathbf{P}'_{\mathcal{F}} = \mathbf{P}_{\mathcal{F}}\mathbf{R}$;
     where
    $$\mathbf{R} = \begin{cases} \mathbf{R}_{\mathbf{x}}(\theta), & \text{ledge test} \\ \mathbf{R}_{\mathbf{y}}(\theta), & \text{rotating drum} \end{cases}$$
    Compute layer thickness (along z'-axis):
    for *each bin size* $b \in \mathbf{B}$ **do**
      divide the x'-axis into K bins of width b.
      for *each bin* $k = 1, \dots, K$ **do**
        define $\mathcal{F}_k$ as the set of flowing particles in bin k.
        compute local thickness: $t_k = \max(z'_i) - \min(z'_i), \quad i \in \mathcal{F}_k$
      $h_b = \frac{1}{K} \sum_{k=1}^{K} t_k$
    $h = \text{median}_{b\in\mathbf{B}}(h_b)$
    Mean particle diameter:
    $d = \frac{1}{|\mathcal{F}|} \sum_{i\in\mathcal{F}} d_i$;
    Mean particle speed:
    $\bar{V} = \frac{1}{|\mathcal{F}|} \sum_{i\in\mathcal{F}} v_{\mathcal{F},i}$;

Data availability

Raw data, processing scripts, and other supportive data is stored in a data repository, referenced in the article.

References

[1] S. Chin, J. Vincent, N.F. Razak, N. Daud, S. Chowdhury, C. Wongchoosuk, C.H. Chia, Advancements and challenges in sodium borohydride hydrogen storage: A comprehensive review of hydrolysis, regeneration, and recycling technologies, J. Renew. Sustain. Energy (ISSN: 1941-7012) 17 (1) (2025) 012702, http://dx.doi.org/10.1063/5.0242699.

[2] D. Santos, C. Sequeira, Sodium borohydride as a fuel for the future, Renew. Sustain. Energy Rev. (ISSN: 1364-0321) 15 (8) (2011) 3980–4001, http://dx.doi.org/10.1016/j.rser.2011.07.018.

[3] Y. Zhu, L. Ouyang, H. Zhong, J. Liu, H. Wang, H. Shao, Z. Huang, M. Zhu, Closing the loop for hydrogen storage: Facile regeneration of $NaBH_4$ from its hydrolytic product, Angew. Chem. 132 (22) (2020) 8701–8707, http://dx.doi.org/10.1002/ange.201915988, (ISSN: 0044-8249, 1521-3757).

[4] E. van Rheenen, J. Padding, A. Kana, K. Visser, Ship system design changes for the transition to hydrogen carriers, Int. Mar. Des. Conf. (ISSN: 3050-4864) (2024) http://dx.doi.org/10.59490/imdc.2024.894.

[5] E. van Rheenen, J. Padding, C. Slootweg, K. Visser, A review of the potential of hydrogen carriers for zero emission, low signature ship propulsion systems, in: Conference Proceedings of INEC, 2022, http://dx.doi.org/10.24868/10649.

[6] E. van Rheenen, J. Padding, A. Kana, K. Visser, Comparative energy analysis of hydrogen carriers as energy source on ships, J. Mar. Eng. Technol. (ISSN: 2046-4177) (2025) 1–15, http://dx.doi.org/10.1080/20464177.2024.2448057.

[7] M. van Benten, J. Padding, D. Schott, Circular bunkering for maritime vessels using sodium borohydride, Renew. Sustain. Energy Rev. (ISSN: 1364-0321) 223 (2025) 116039, http://dx.doi.org/10.1016/j.rser.2025.116039.

[8] M. van Benten, J. Padding, D.L. Schott, Experimental characterization of granular sodium borohydride under varying operational conditions across flow regimes, Powder Technol. (ISSN: 0032-5910) 469 (2026) 121739, http://dx.doi.org/10.1016/j.powtec.2025.121739.

[9] G. Midi, On dense granular flows, Eur. Phys. J. E (ISSN: 1292-8941) 14 (4) (2004) 341–365, http://dx.doi.org/10.1140/epje/i2003-10153-0.

[10] Y. Nagar, A. Schechter, B. Ben-Moshe, N. Shvalb, Modeling the mechanical behavior of sodium borohydride ($NaBH_4$) powder, Mater. Des. (ISSN: 02641275) 108 (2016) 240–249, http://dx.doi.org/10.1016/j.matdes.2016.06.077.

[11] I. Govender, Granular flows in rotating drums: A rheological perspective, Miner. Eng. (ISSN: 0892-6875) 92 (2016) 168–175, http://dx.doi.org/10.1016/j.mineng.2016.03.021.

[12] M. van Benten, J. Padding, D. Schott, Data for modelling free-flowing sodium borohydride in the dense flow regime using DEM [dataset], 4TU.ResearchData, 2025, http://dx.doi.org/10.4121/6876266d-60dd-4df2-b57f-88c14b57733c.

[13] Altair EDEM, Base contact models, https://help.altair.com/edem.

[14] T. Roessler, C. Richter, A. Katterfeld, F. Will, Development of a standard calibration procedure for the DEM parameters of cohesionless bulk materials – Part I: Solving the problem of ambiguous parameter combinations, Powder Technol. (ISSN: 0032-5910) 343 (2019) 803–812, http://dx.doi.org/10.1016/j.powtec.2018.11.034.

[15] C. Wensrich, A. Katterfeld, Rolling friction as a technique for modelling particle shape in DEM, Powder Technol. (ISSN: 0032-5910) 217 (2012) 409–417, http://dx.doi.org/10.1016/j.powtec.2011.10.057.

[16] J. Ai, J. Chen, J. Rotter, J. Ooi, Assessment of rolling resistance models in discrete element simulations, Powder Technol. (ISSN: 0032-5910) 206 (3) (2011) 269–282, http://dx.doi.org/10.1016/j.powtec.2010.09.030.

[17] C. Jiang, X. An, M. Li, Y. Wu, D. Gou, Y. Wu, DEM modelling and analysis of the mixing characteristics of sphere-cylinder granular mixture in a rotating drum, Powder Technol. (ISSN: 0032-5910) 426 (2023) 118653, http://dx.doi.org/10.1016/j.powtec.2023.118653.

[18] G. Chen, Y. Mei, Y. Zhang, B. Jin, DEM investigation on flow regime transition of cylindrical particle in a rotating drum, Int. J. Chem. React. Eng. (ISSN: 1542-6580) 22 (8) (2024) 893–912, http://dx.doi.org/10.1515/ijcre-2024-0029.

[19] T. Povall, I. Govender, A. McBride, Dense granular flows in rotating drums: A computational investigation of constitutive equations, Powder Technol. (ISSN: 0032-5910) 393 (2021) 238–249, http://dx.doi.org/10.1016/j.powtec.2021.07.051.

[20] R. Chand, M. Khaskheli, A. Qadir, B. Ge, Q. Shi, Discrete particle simulation of radial segregation in horizontally rotating drum: Effects of drum-length and non-rotating end-plates, Phys. A 391 (2012) 4590–4596, http://dx.doi.org/10.1016/j.physa.2012.05.019.

[21] G. Chen, G. Lodewijks, D. Schott, Surface Wear Reduction of Bulk Solids Handling Equipment Using Bionic Design (Ph.D. thesis), Delft University of Technology, 2017, http://dx.doi.org/10.4233/UUID:B60CB231-222D-434D-B987-CF36605BC719.

[22] Altair EDEM, Discrete element modeling - DEM software, https://altair.com/edem.

[23] T. Ghellab, Z. Charifi, H. Baaziz, H. Latteli, M. Güler, c. Uğur, E. Güler, G. Uğur, The elastic, mechanical, and thermodynamic properties of NaXH4 (X=B, Al) intended for the storage of hydrogen: An ab-initio study, Phys. B (ISSN: 0921-4526) 638 (2022) 413851, http://dx.doi.org/10.1016/j.physb.2022.413851.

[24] S. Lommen, D. Schott, G. Lodewijks, DEM speedup: Stiffness effects on behavior of bulk material, Particuology (ISSN: 1674-2001) 12 (2014) 107–112, http://dx.doi.org/10.1016/j.partic.2013.03.006.

[25] S. Pourandi, P. Van Der Sande, T. Weinhart, I. Ostanin, A mathematical model for the dynamic angle of repose of a granular material in the rotating drum, Powder Technol. (ISSN: 00325910) 446 (2024) 120176, http://dx.doi.org/10.1016/j.powtec.2024.120176.

[26] GranuDigitalTwins / GranuDrum digital twin - EDEM from Altair · GitLab, 2025, https://gitlab.com/gdigitaltwins/granudrum-digital-twin-edem-from-altair,

[27] A. Hadi, Y. Pang, D. Schott, Systematic DEM calibration of two-component mixtures using AI-accelerated surrogate models, Powder Technol. (ISSN: 0032-5910) 464 (2025) 121190, http://dx.doi.org/10.1016/j.powtec.2025.121190.

[28] F. Da Cruz, S. Emam, M. Prochnow, J.-N. Roux, F. Chevoir, Rheophysics of dense granular materials: Discrete simulation of plane shear flows, Phys. Rev. E - Stat. Nonlinear, Soft Matter Phys. (ISSN: 1550-2376) 72 (2) (2005) http://dx.doi.org/10.1103/PhysRevE.72.021309.

[29] J. Mellmann, The transverse motion of solids in rotating cylinders—Forms of motion and transition behavior, Powder Technol. (ISSN: 0032-5910) 118 (3) (2001) 251–270, http://dx.doi.org/10.1016/S0032-5910(00)00402-2.

[30] D. Santos, R. Scatena, C. Duarte, M. Barrozo, Transition phenomenon investigation between different flow regimes in a rotary drum, Braz. J. Chem. Eng. 33 (2016) 491–501, http://dx.doi.org/10.1590/0104-6632.20160333s20150128, (ISSN: 0104-6632, 1678-4383).

[31] S. Derakhshani, D. Schott, G. Lodewijks, Micro–macro properties of quartz sand: Experimental investigation and DEM simulation, Powder Technol. (ISSN: 0032-5910) 269 (2015) 127–138, http://dx.doi.org/10.1016/j.powtec.2014.08.072.